


FULL PAPER

Open Access



A new infrared volcano monitoring using GCOM-C (SHIKISAI) satellite: applications to the Asia-Pacific region

Takayuki Kaneko^{1*} , Atsushi Yasuda¹, Kenji Takasaki², Shun Nakano³, Toshitsugu Fujii⁴, Yoshiaki Honda⁵, Kouji Kajiwara⁵ and Hiroshi Murakami⁶

Abstract

The GCOM-C (SHIKISAI) satellite was developed to understand the mechanisms of global climate change. The second-generation global imager (SGLI) onboard GCOM-C is an optical sensor observing wavelengths from 380 nm to 12.0 μm in 19 bands. One of the notable features is that the resolution of the 1.63, 10.8, and 12.0 μm bands is 250 m, with an observation frequency of 2–3 days. To investigate the effective use and potential of the 250 m resolution of these SGLI bands in the study of eruptive activities, we analyzed four practical cases. As an example of large-scale effusive activity, we studied the 2018 Kilauea eruption. By analyzing the series of 10.8 μm band images using cumulative thermal anomaly maps, we could observe that the lava effused on the lower East Rift Zone, initially flowed down the southern slope to the sea, and then moved eastward. As an example of lava dome growth and generation of associated pyroclastic flows, the activity at Sheveluch between December 2018 and December 2019 was analyzed. The 1.63 and 10.8 μm bands were shown to be suitable for observing growth of the lava dome and occurrence of pyroclastic flows, respectively. We found that the pyroclastic flows occurred during periods of rapid lava dome expansion. For the study of an active crater lake, the activity of Ijen during 2019 was analyzed. The lake temperature was found to rise rapidly in mid-May and reach 38 °C in mid-June. We also analyzed the intermittent activities of small-scale vulcanian eruptions at Sakurajima in 2019. The 1.63 μm band was useful for detecting activities that are associated with vulcanian eruptions. Analytical results for these case studies demonstrated that the GCOM-C SGLI images are beneficial for observing various aspects of volcanic activity, and their real-time use may contribute to reducing eruption-related disasters.

Keywords: GCOM-C, SGLI, SHIKISAI, Volcano, Eruption, Remote sensing

Introduction

The Global Change Observation Mission-Climate (GCOM-C, SHIKISAI) satellite was developed by the Japan Aerospace Exploration Agency (JAXA) and successfully launched in December 2017. The second-generation global imager (SGLI) mounted on GCOM-C is an optical sensor that observes the wavelength range from near ultraviolet to thermal infrared

(380 nm –12.0 μm) with 19 bands having resolution of 250 m to 1 km. The SGLI can observe the same area of the earth every 2–3 days (JAXA 2018a; Tanaka et al. 2010). The primary purpose of the GCOM-C project is to observe and understand the mechanisms of heat flow in the earth and the distribution of ecosystem changes due to global warming, and further use the obtained knowledge to improve the numerical models that predict future climate change (Imaoka et al. 2010; JAXA 2018a).

The GCOM-C SGLI system was not necessarily designed to be applied to volcano observation. SGLI,

*Correspondence: kaneko@eri.u-tokyo.ac.jp

¹ Earthquake Research Institute, The University of Tokyo, 1-1-1 Yayoi, Bunkyo-ku, Tokyo 113-0032, Japan

Full list of author information is available at the end of the article

however, has two significant advantages for volcano observation: the resolution of the infrared bands at 1.63, 10.8, and 12.0 μm is 250 m and the observation frequency is relatively high—about the same level as the NASA Moderate Resolution Imaging Spectroradiometer (MODIS) (JAXA 2018a). By applying this distinctive satellite imaging capability to volcanic infrared surveys, we can obtain useful information that cannot be gathered by other satellites, which might greatly contribute to advances in volcano observation.

The objectives of this study were to investigate how representative eruptive or deposition activities are seen in SGLI images, what kinds of activities or deposits are suitable for being observed with the SGLI, and then what kinds of methods we should adopt to analyze volcanoes using SGLI images. Therefore, we worked on analyzing several different types of activities, selected from the observation data acquired during 2018–2019. Through the analyses of these practical cases, we investigated effective measures and systems for using SGLI images in the study of eruptive processes and eruption sequences, as well as disaster mitigation. Here, as analysis examples, we examined a large-scale effusive activity (2018 Kilauea eruption), lava dome growth and generation of associated pyroclastic flows (2018–2019 Sheveluch activity), an active volcanic crater lake (2019 Ijen activity), and intermittent small-scale vulcanian eruptions (2019 Sakurajima activity). It is crucial to summarize early results of eruption observations using SGLI images at this point 2 years after the launch of GCOM-C, to promote the use of SGLI images in the field of volcano observation, and also to inform the specifications of the next version of the SGLI.

Materials and methods

Characteristics of GCOM-C SGLI suitable for volcano observation

The GCOM-C satellite orbits at an altitude of about 798 km in a Sun-synchronous sub-recurrent orbit with an inclination of 98.6° and Local Solar Time at the descending node of $10:30 \pm 15$ (Imaoka et al. 2010; JAXA 2018a; Tanaka et al. 2010). GCOM-C transitioned to regular operation in December 2018, and SGLI data have been provided to general users since then. SGLI has an observation width of about 1400 km (in the case of infrared bands) and can observe the same point on the earth every 2–3 days at both day and night. The SGLI consists of a visible and near-infrared radiometer (SGLI-VNR) and an infrared scanning radiometer (SGLI-IRS) (JAXA 2018a; Tanaka et al. 2018). Table 1 gives the specifications of the SGLI-IRS used in this study (Tanaka et al. 2014).

To make infrared observation of volcanoes using the SGLI, we have to consider the following three points;

the highest spatial resolution is 250 m, the bands with 250 m resolution are limited to wavelengths of 1.63 μm , 10.8 μm and 12.0 μm , and the observation frequency is every 2–3 days at night. The 12.0 μm band is not used in this study, because its characteristics are similar to those of the 10.8 μm band and the split window method is not adopted here; it is omitted from the discussion hereafter.

Characteristics of the 1.63 μm and 10.8 μm bands for volcano observation

Using the Planck equation, we reconfirmed the characteristics of the 1.63 μm and 10.8 μm wavelength regions for the relationship between temperature and spectral radiance (Fig. 1a, b). At 10.8 μm , the spectral radiance shows a nearly linear relationship with temperature (Fig. 1a). For this reason, the spectral radiance reflects the temperature of portions occupying large areas within a pixel (Wooster and Rothery 1997). Also, the radiance is sufficient, even at low temperatures (Fig. 1b). Conversely, even if there is a high-temperature heat source exceeding 700–800 $^\circ\text{C}$ within a pixel, it has virtually no effect on the spectral radiance value of the pixel when its area is less than 0.2–0.3% (Fig. 1c). At 1.63 μm , the spectral radiance is low at low temperatures, close to the background, but it significantly increases at higher temperatures exceeding several hundred degrees Celsius (Fig. 1a, b). Therefore, in the case where a high-temperature heat source exceeding several hundred degrees Celsius exists within a pixel, even if the area is minimal, the pixel can show a thermal anomaly (Fig. 1c) (Wooster and Rothery 1997).

Availabilities of the SGLI 1.63 μm and 10.8 μm bands for volcano observation

The 1.63 μm and 10.8 μm bands of SGLI have the following availabilities for volcano observation:

Observation of distribution of erupted materials Lava flows and pyroclastic flows commonly have a scale of a few kilometers. With the 250 m resolution of the SGLI,

Table 1 Specifications of the InfraRed Scanning Radiometer (SGLI-IRS).

Band	Wavelength	Resolution
SW1	1.05 μm	1000 m
SW2	1.38 μm	1000 m
SW3	1.63 μm	250 m
SW4	2.21 μm	1000 m
T1	10.8 μm	250 m
T2	12.0 μm	250 m

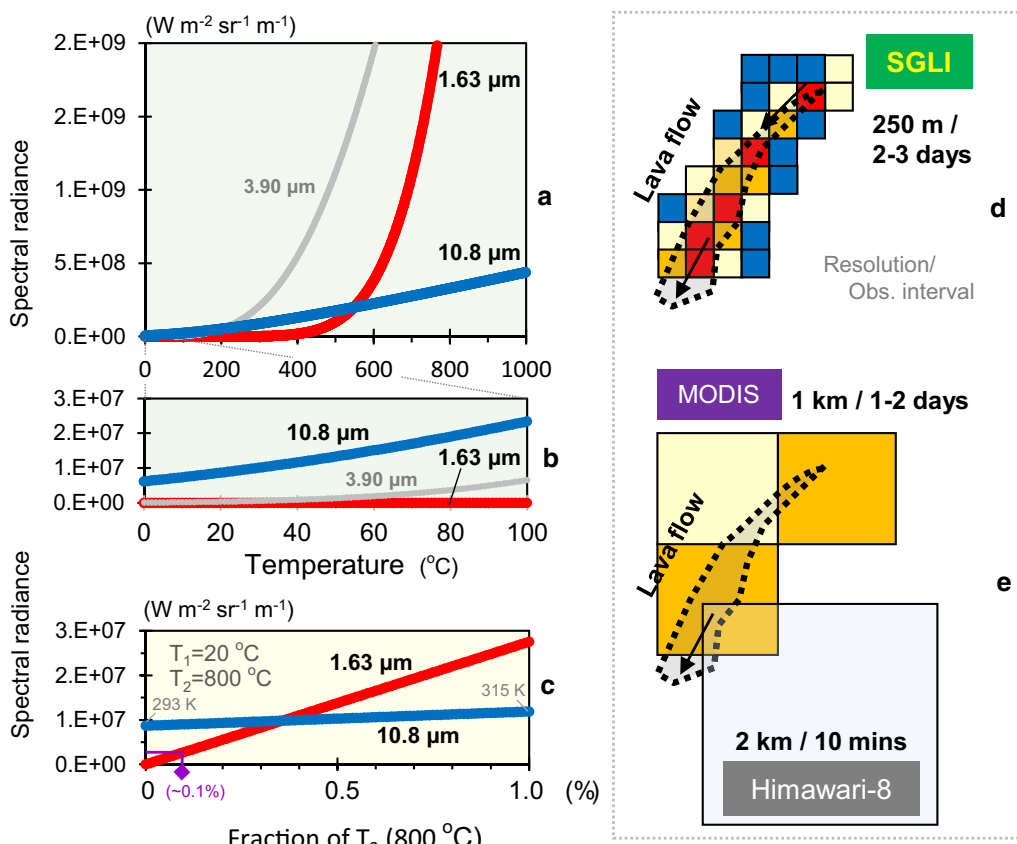


Fig. 1 **a, b** Relationship between temperature and spectral radiance based on the Planck equation. **c** Relationship between fraction of high-temperature portion within a pixel (%) and spectral radiance at 1.63 μm and 10.8 μm. The high-temperature portion (T_2) and the background (T_1) are assumed to be 800 °C and 20 °C, respectively. **d** Schematic illustration of the relationship between pixel size of the SGLI and a small to medium lava flow. **e** Schematic illustration showing the relationship between pixel size of the MODIS and Himawari-8 and a small to medium lava flow

we can identify the distribution of such deposits (Fig. 1d). With MODIS or Himawari-8 having a large pixel size (1 km and 2 km, respectively), it is difficult to grasp the distribution unless the scale of the deposit is enormous (Fig. 1e). Because the surface temperature of pyroclastic and lava flows generally fall below 100 °C within a few days after deposition, the 10.8 μm band of SGLI is thought to be suitable for capturing the distribution of deposits due to the presence of thermal anomalies.

Temperature measurement of near-homogeneous temperature regions The 10.8 μm band of the SGLI is valid for the surface temperature measurement of a near-homogeneous temperature region with a slightly lower temperature range (maximum 340 K; JAXA 2018a), such as lava or pyroclastic flows after a few days of settlement.

Time-series variation of distribution areas The SGLI can detect the distribution areas of erupted materials with a

relatively high observation frequency (every 2–3 days). For this reason, it is possible to observe the time-series variation in the distribution of erupted materials. This is the most significant advantage of the SGLI over other satellite imagers.

Observation of sub-pixel small heat sources Because the SGLI has a small pixel size, the proportion of the volcanic heat source in a pixel becomes relatively large, which makes it possible to detect small-scale heat sources. In particular, the 1.63 μm band, which shows high spectral radiance in the high-temperature region, is suitable for observation of small-scale high-temperature heat sources (Fig. 1c), such as magma slightly exposed at the bottom of a crater.

Data processing

All the SGLI images used in this study were created with nighttime data according to the procedure in this

subsection. Level 1B images of SGLI-IRS (short-wave infrared bands SW1, SW2, SW3, and SW4 and thermal infrared bands T1 and T2) were downloaded from the data server at JAXA (G-Portal, <https://gportal.jaxa.jp/gpr/index/index?lang=ja>). The DN (digital number) values of the images were converted to spectral radiance using the conversion coefficients given in the header (JAXA 2018b). Geometric correction was performed by resampling using the NN (nearest neighbor) method and the latitude and longitude information included in the data (JAXA 2018b). After that, areas of 801 pixels (latitude direction) by 401 pixels (longitude direction) centered on the target volcanos were cut out. The conversion from spectral radiance to pixel-integrated temperature was performed with the Planck equation (e.g., Rothery et al. 1988). Atmospheric corrections were performed for the values of spectral radiance and pixel-integrated temperature using the correction coefficients obtained by MODTRAN3_7 (Berk et al. 1989). The emissivity for water surface and basaltic to andesitic rocks in the 10.8 μm band was assumed to be 0.95 with reference to Walter and Salisbury (1989) and Harris (2013). The same value was adopted for the 1.63 μm band. Table 2 summarizes the models and coefficients for the atmospheric correction and emissivity used in the study of each volcanic activity. To define thermal anomalies in the 1.63 μm images, the spectral radiance of the pixel showing the highest value in the heat source area was used, and to define them in the 10.8 μm images, the pixel-integrated temperature was used (hereafter referred to as “R1.6Mx” and “T11Mx,” respectively). The details of the correction methods and the thermal anomaly indicators are described in Kaneko et al. (2018).

Analysis of four representative eruptive cases

2018 Kilauea eruption—large-scale effusive activity

Outline of the 2018 Kilauea eruption and analytical points

Kilauea is a shield volcano with an altitude of 1247 m located in southeastern Hawaii Island, and it is the most active volcano in the Hawaiian Islands chain (Fig. 2a). In addition to eruptions at the summit, fissure eruptions frequently occur along the East Rift Zone (ERZ) and the Southwest Rift Zone extending from the summit (Macdonald et al. 1983). The eruption sequence of the 2018 activity has been reported in detail by the U.S. Geological Survey (USGS 2018) and Neal et al. (2019). This eruption is thought to have resulted from migration of a part of the magma below the Kilauea Caldera to the east through the ERZ, which caused the eruptions at the lower ERZ and collapses at the summit area (Feng et al. 2020; Neal et al. 2019).

The outline of the eruptive sequence is as follows (Fig. 2a, b). On 30 April, a collapse occurred at the Pu’u ‘Ō’ō Crater in the middle of the ERZ. On 3 May, a fissure eruption began at the foot of the lower ERZ. On 10 May, the lava lake in the Halema’uma’u Crater within the Kilauea Caldera disappeared, and on 16 May, an explosive eruption took place in this crater. Lava flows effused from the fissures on 19 May and headed to the sea; that night, lava entered the sea near MacKenzie State Recreation Area (ocean entry). On 3 June, lava that flowed east from Fissure 8 buried the Kapoho Crater and flowed into Kapoho Bay (ocean entry). The lava had completely filled Kapoho Bay by 5 June. From then until mid-June, the inflow of lava enlarged the land around Kapoho Bay toward the sea. In mid-July, the lava effused from Fissure 8 began to flow toward the area south of Kapoho Crater. On 4 August, lava effusion decreased rapidly.

In observing the eruption sequence of effusive eruptions, the prime issue is to monitor the enlargement of the areas covered by lava flows. In this study, we observed

Table 2 Models and coefficients for the atmospheric correction and emissivity used in each study

Activity	MODTRAN model	1.63 μm atmospheric transmittance	10.8 μm atmospheric transmittance	10.8 μm upwelling atmospheric radiance (W m ⁻² sr ⁻¹ m ⁻¹)	Emissivity
2018 Kilauea	Tropical, Altitude = 0.2 km	–	0.54	3.76 × 10 ⁶	0.95
2018–2019 Sheveluch (Lava dome/chart)	1976 US Standard, Altitude = 2.5 km	0.98	0.96	2.01 × 10 ⁵	0.95
2018–2019 Sheveluch (Whole area/images)	1976 US Standard, Altitude = 1.0 km	0.96	0.90	5.61 × 10 ⁵	0.95
2019 Ijen	Tropical, Altitude = 2.2 km	–	0.87	8.92 × 10 ⁵	0.95
2019 Sakurajima	1976 US Standard, Altitude = 1.0 km	0.96	0.90	5.61 × 10 ⁵	0.95

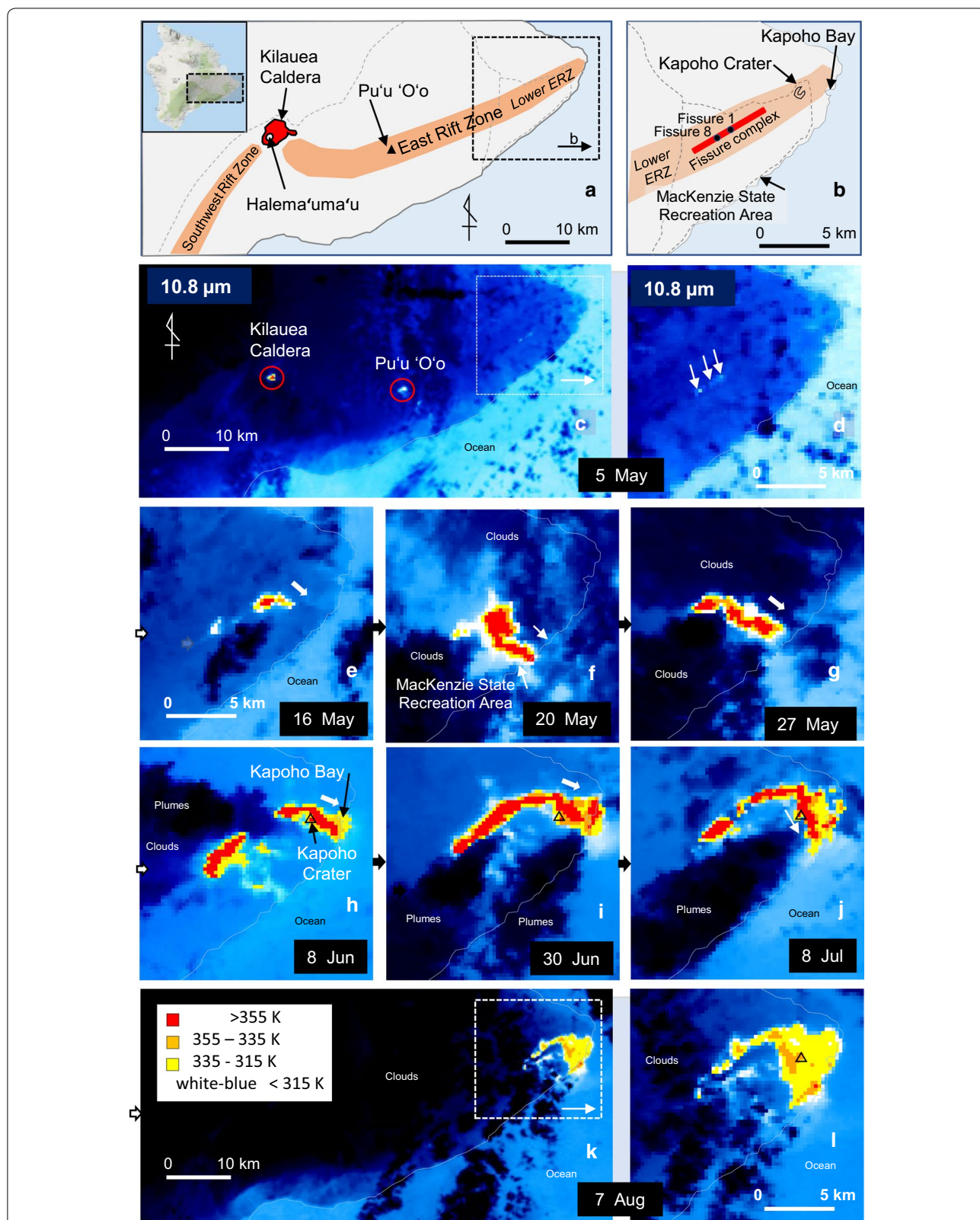


Fig. 2 **a** Location of the Kilauea Caldera and East Rift Zone. **b** Lower ERZ and surrounding areas. **c–l** Eruptive sequence of the 2018 Kilauea eruption observed with 10.8 μm images from the SGLI (pixel-integrated temperature)

the time-series evolution of the covered area with the SGLI 10.8 μm images. In this case, although active areas with high temperatures at the time of imaging can be detected, it is difficult to grasp the whole picture of the eruption sequence through the entire active period. To deal with this problem, we developed a method we called the “cumulative thermal anomaly map.” The cumulative thermal anomaly map records the location of the pixels that showed thermal anomalies at least once during the activity period and cumulatively sums them from the start of the activity to the time of the current observation. A location showing a thermal anomaly at least once can be interpreted as a point where lava is effusing or flowing. Even when a pixel with a thermal anomaly is covered with clouds or plumes at the time of imaging by the SGLI, the pixel can be included in the covered area if it still shows a thermal anomaly at the next imaging opportunity. Therefore, by constructing a cumulative thermal anomaly map, it is possible to understand how the lava flows have been enlarging and where the lava is effusing from and flowing toward comprehensively. In this study, pixels with a pixel-integrated temperature higher than the threshold of 335 K were extracted as the distribution areas of active lava flows.

Results for 2018 Kilauea eruption

First, we evaluated the eruptive progression using images of the pixel-integrated temperature of the SGLI 10.8 μm band (Fig. 2c–l). In the image of 5 May (UTC), weak thermal anomalies are recognized in the lower ERZ at an altitude of about 200 m, aligned in the same direction as the extension of the ERZ (Fig. 2d). These are thought to be the locations where the initial fissure eruptions occurred. Thermal anomalies are also recognized at the Halema'uma'u Crater in the Kilauea Caldera and the Pu'u 'Ō'ō Crater where collapses occurred (Fig. 2c). In the 16 May (UTC) image, the areas showing thermal anomalies have enlarged and extended to the east-northeast, suggesting that the activity is increasing (Fig. 2e). In the images of late May (Fig. 2f, g), lava flowing down the slope to the southeast has reached the coast near MacKenzie State Recreation Area and flowed into the sea (ocean entry was on 19 May; USGS 2018). After this, the image from 8 June (Fig. 2h) shows that lava flows are heading east from the vicinity of the first eruption sites, have buried Kapoho Crater, and are flowing into Kapoho Bay (ocean entry was on 3 June; USGS 2018). The images of 30 June, 8 July, and 7 August show that lava flowed into the southern region of the Kapoho Crater, and the distribution areas of lava are being gradually enlarged to the south (Fig. 2i–l).

Figure 3a shows the cumulative thermal anomaly maps produced from the series of SGLI images. Based on these maps, we can systematically understand the sequence of

the enlargement process of the lava flows throughout the activity. The lava generated by the eruption on the lower ERZ initially flowed down the southern slope to the sea, and then moved eastward and buried the Kapoho Crater and Kapoho Bay and its surroundings. The cumulative thermal anomaly map for 7 August agrees well with the actual distribution of the lava flows reported on the 7 August map by USGS (2018) (Fig. 3b). However, the distribution in the vicinity of the fissure zone in our map is much broader than it actually is. This is due to misalignment between images used for the cumulative thermal anomaly maps, the possibility that the high-temperature part of a plume was misidentified as a lava flow, and a parallax view from the satellite resulting from the altitude of the fissure zone (100–300 m above sea level). Figure 3c shows the temporal change in the distribution area of the lava flows, and Fig. 3d shows the temporal variation of lava flows over the coverage area; both of them were produced from the series of cumulative thermal anomaly maps. Coverage by the lava flows increased almost in proportion with time from mid-May to early June, but started to slow down in July and leveled off in August. The distribution area of the lava as of 7 August was measured to be 35.5 km² (USGS 2018); however, the area of the same day calculated from the cumulative thermal anomaly map is about 50 km², which is almost 1.4 times wider. This is thought to be mainly due to the error factors listed above.

Discussion of 2018 Kilauea eruption

The lava flows produced by the 2018 Kilauea eruption covered an area of 35.5 km² (USGS 2018), which significantly exceeds the pixel size of the SGLI; thus, we could detect the distribution of the lava flows and the time-series variation of its enlargement using the SGLI images. The probability of occurrence of large-scale eruptions (e.g., erupted volume > $\sim 10^9$ m³) is not very high; however, in addition to the Kilauea eruption, similar significant eruptions recently occurred in the Tolbachik volcano on the Kamchatka Peninsula in 2012 (Edwards et al. 2013) and the Wolf volcano in Galapagos in 2015 (Wright et al. 2015). The 864–866 eruption of Mt. Fuji (Takada et al. 2014) is another example of this type. In future eruptions of this type, if the cumulative thermal anomaly maps are produced using SGLI images in real time, we can also grasp the distribution and enlargement process of the lava flows as they occur, which is highly useful for disaster prevention. However, when observing the distribution of lava flows at a higher altitude, the parallax effect appears strongly in Level 1b images of SGLI, so it is necessary to perform parallax correction or use L2 LTOA (level-2 top-of-atmosphere radiance) images—precise geometric correction has been made through the

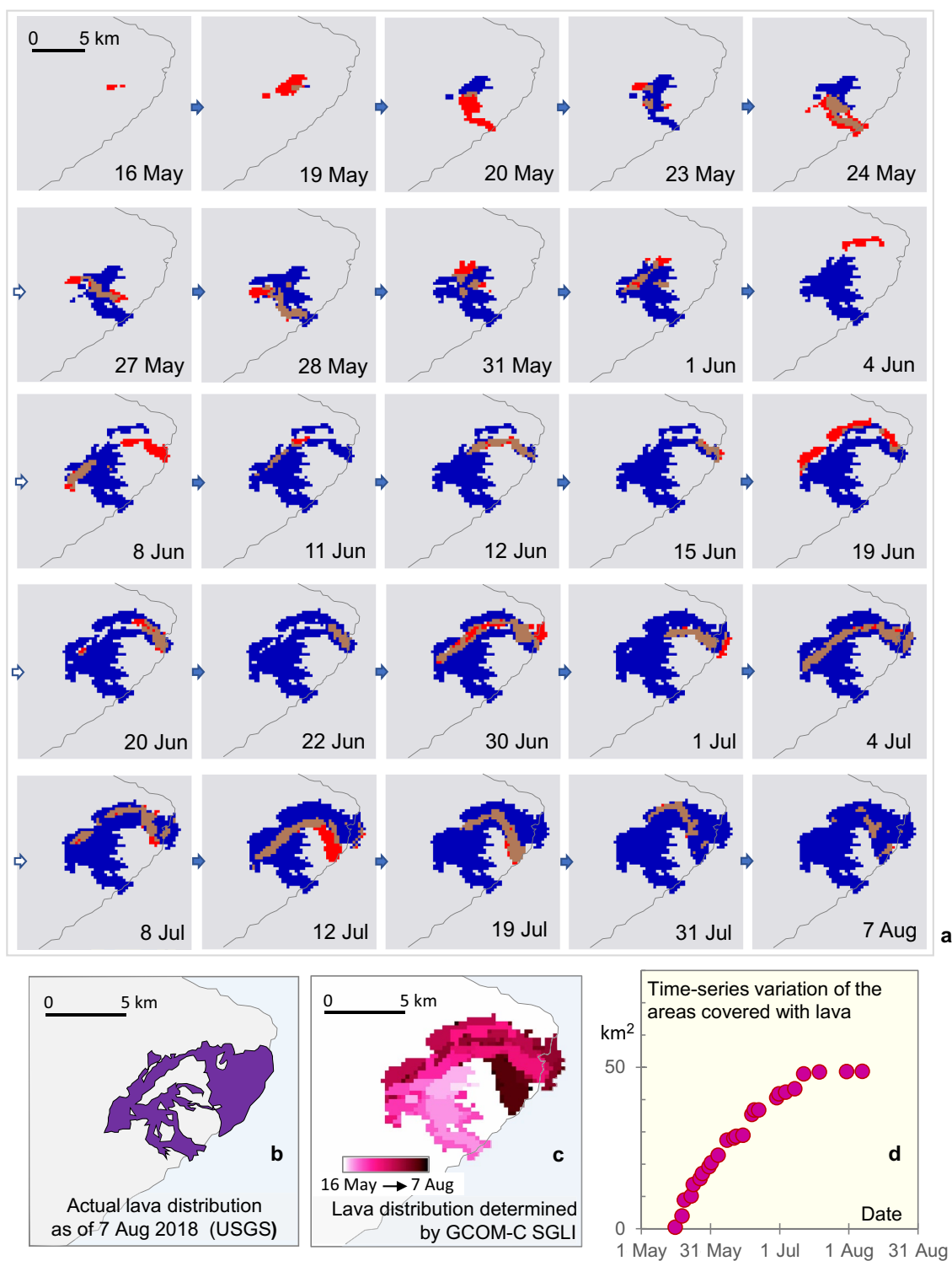


Fig. 3 **a** Cumulative thermal anomaly map of the 2018 Kilauea lava flows produced from a series of SGLI images. Red: Newly effused active lava on the original ground surface; Brown: Newly effused active lava on the settled 2018 lava; Blue: Settled 2018 lava; Light Gray: Original ground surface. **b** Actual lava distribution on 7 August 2018, as reported by USGS (USGS 2018). **c** Temporal change in the distribution area of the lava flows based on the cumulative thermal anomaly maps. **d** Temporal variation in the area covered by lava flows based on the cumulative thermal anomaly maps

ortho-rectification by the digital elevation model and the ground control points (JAXA 2018b).

2018–2019 Sheveluch activity—lava dome growth and generation of associated pyroclastic flows

Outline of the 2018–2019 Sheveluch activity and analytical points

Sheveluch volcano, which has an altitude of 3283 m, is the northernmost of the active volcanoes on the Kamchatka Peninsula, Russia, and is one of the most active volcanoes in the world (Fig. 4a–c). Sheveluch volcano consists of Old Sheveluch and Young Sheveluch. At Young Sheveluch, eight large-scale collapses occurred due to lava dome growth and the last collapse was in 1964 (Belousov et al. 1999). Recent activity has also been characterized by smaller scale lava dome growth and the occurrence of pyroclastic flows associated with its collapse (Krippner et al. 2018). In this study, we examined the activities from December 2018 to December 2019.

Observation of pyroclastic flows requires a high observation frequency and reasonably high resolution. The SGLI images with a resolution of 250 m and an observation frequency of 2–3 days could roughly capture the occurrence and distribution of these flows.

In this study, the occurrence of pyroclastic flows was determined by visual interpretation of all 10.8 μm band images during the observation period. In contrast, the time-series variation of the activity level of the lava dome was estimated using the 1.63 μm band images. In each image of Sheveluch, the pixel with the highest value out of the 61-pixel (latitude direction) by 41-pixel (longitudinal direction) area centering on the lava dome was extracted, and the radiance value (R1.6Mx) was used to identify thermal anomalies (Kaneko et al. 2018). Because the 1.63 μm wavelength region is insensitive to hot spots below several hundred degrees Celsius (Fig. 1a, b), thermal anomalies resulting from the growing lava dome can be selectively detected without being affected by incidental deposits with a lower surface temperature (Kaneko et al. 2002a), such as talus deposits caused by a small collapse of the lava dome (Shevchenko et al. 2015) or pyroclastic flows.

Results for 2018–2019 Sheveluch activity

Generation and distribution of pyroclastic flows An intensive investigation of the SGLI images acquired between December 2018 and December 2019 revealed that pyroclastic flows were captured in the images of 30 December 2018 and 2 September 2019 (Fig. 4d–g). In between, no pyroclastic flow was observed to occur—the collapsed materials accumulated exclusively as a talus around the lava dome (Shevchenko et al., 2015) and did not evolve into a pyroclastic flow. In the image on 30 Decem-

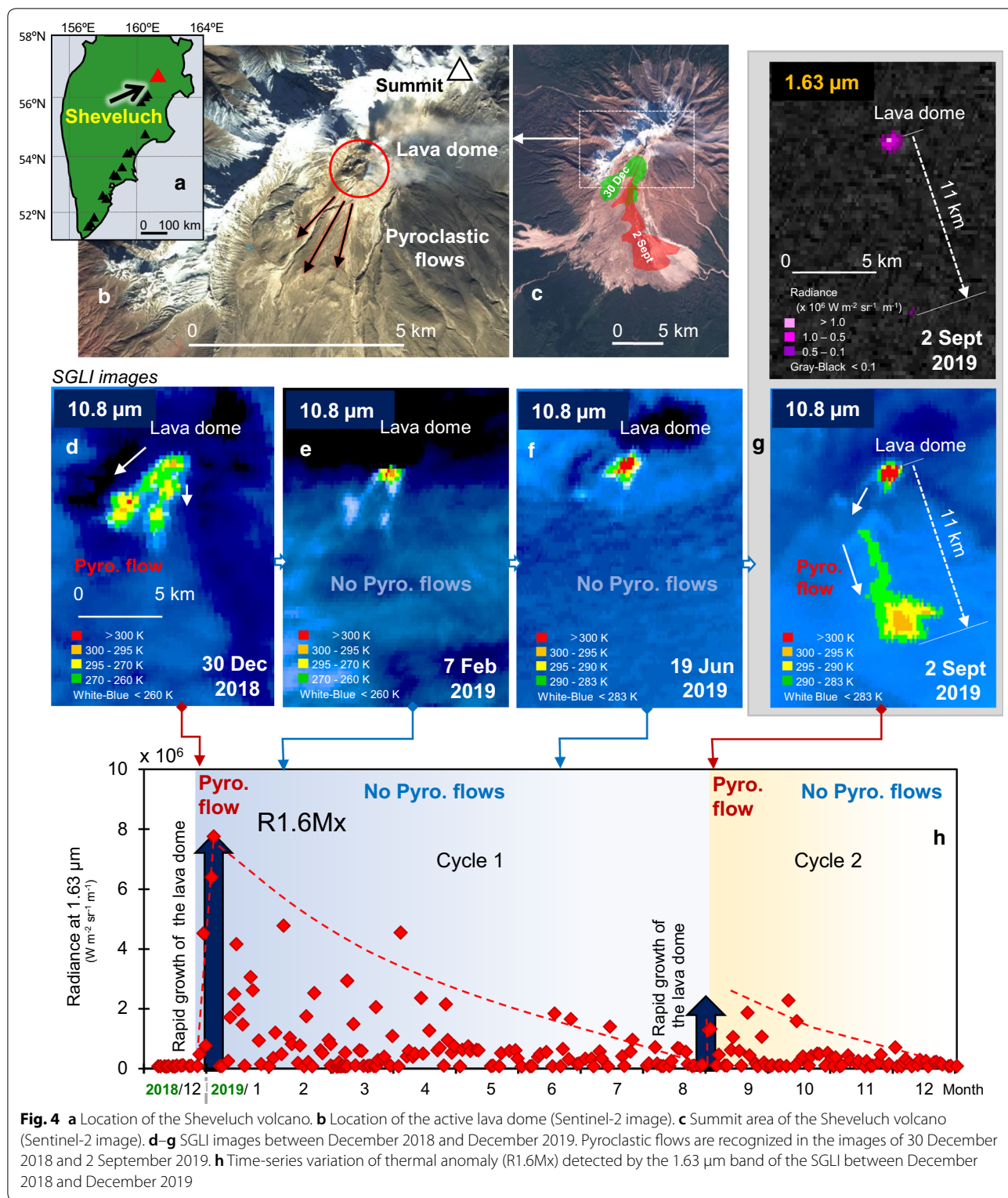
ber 2018 (Fig. 4d), a bifurcated pyroclastic flow extends about 5 km southwest from the lava dome. The pyroclastic flow seen in the image on 2 September 2019 (Fig. 4g) traveled 11 km to the south. The latter is twice as long as the most abundant pyroclastic flow generated in the 1995 Unzen eruption (Nakada et al. 1999); however, it corresponds to the medium size among the recent pyroclastic flows in Sheveluch. The pyroclastic flow that occurred in October 2010 traveled 19 km downslope (Krippner et al. 2018). The lava dome shows thermal anomalies in both the 1.63 μm and 10.8 μm images, but pyroclastic flow is visible only in the 10.8 μm images and is not captured in the 1.63 μm images except for a few pixels at the tip of the flow (Fig. 4g). This is probably due to the heat loss during the pyroclastic flowing process and the cooling of the surface after deposition. In the 10.8 μm image, the pyroclastic flow front is at 295–300 K, which is a dozen degrees higher than temperatures in the surrounding areas, suggesting that the pyroclastic flow is thick in this area.

Time-series variation of thermal anomaly relating to the lava dome activity

Figure 4h shows the time-series variation of R1.6Mx from December 2018 to December 2019. The R1.6Mx value increased sharply at the end of December 2018, then decreased monotonically over the next 8 months, but rose sharply again in September 2019. After that, it decreased again with slight fluctuations. As shown in the figure, during this period, the Sheveluch dome twice showed a rapidly increasing and gently decreasing pattern in the thermal anomaly over a time-scale of several months. It is believed that R1.6Mx basically reflects the lava effusion rate (Kaneko et al. 2002a; Kaneko and Wooster, 1999; Wooster and Kaneko 1998); thus, the lava effusion in this period is also inferred to have repeated this time-series variation, that is, the rapid increase and gentle decrease. This observation suggests that the growth rate of the lava dome suddenly changed from slow to fast at the end of December 2018 and also at the beginning of September 2019.

Discussion of 2018–2019 Sheveluch activity

Comparison of the timing of the two pyroclastic flows (Fig. 4d–g) and the time-series variation of the R1.6Mx thermal anomaly (Fig. 4h) shows that the pyroclastic flows occurred near the peaks where the thermal anomaly was increasing rapidly, that is, the growth rate of the lava dome suddenly changed from slow to fast. This fact suggests that a part of the lava dome became unstable due to rapid growth caused by an increase in the lava effusion rate, which finally resulted in large-scale collapse of the lava dome and generation of pyroclastic flows (e.g., Belousov et al. 1999). As another possibility, during the preceding slow growth period, the solidification of a shallow



part of the lava dome had progressed, which caused the accumulation of gas components in the underlying shallow conduit. When the lava effusion increased rapidly,

decompression caused an explosion and the generation of a pyroclastic flow. This sequence might be considered a typical pattern of lava dome evolution involving

vulcanian eruptions. A similar pattern between growth of the lava dome (and also the time-series variation of the thermal anomaly) and the occurrence of vulcanian eruptions was observed in the 1984–1995 Lascar eruptions in Chile (Oppenheimer et al. 1993; Wooster and Rothery 1997).

The 1.63 μm and 10.8 μm images of the SGLI were confirmed to be useful for the observation of lava dome growth and generation of associated pyroclastic flows, respectively. Activities involving lava domes are common in the andesitic to dacitic volcanoes that are common along subduction zones, and the associated pyroclastic flows have often caused fatalities (e.g., 1991 Unzen, 2010 Merapi—central Java island, and 2014 Sinabung). SGLI images, which can observe changes in the lava effusion rate and the presence of pyroclastic flows, can be an essential source of information for studying the mechanism of pyroclastic flow generation from lava dome activities.

2019 Ijen activity—volcanic crater lake

Outline of the 2019 Ijen activity and analytical points

Ijen is a volcanic crater lake formed at an altitude of about 2200 m near the summit of Mt. Merapi, which is located at the eastern end of Java Island, Indonesia (Fig. 5a, b). This volcanic crater lake is 700–900 m in diameter and has a fumarolic area on the southern shore, where sulfur is mined (Caudron et al. 2015). The lake water is strongly acidic with a pH of 0.1, and when activity increases, the temperature of the water rises and bubbles, discolored water, and rising steam are observed (Caudron et al. 2015). In this study, we examined the change in lake surface temperature from January to December 2019.

The point of observation is whether we can measure the temperature of the lake water and monitor the time-series variation with SGLI images having a pixel size of 250 m. The 700–900 m diameter of the lake is slightly larger than $\sqrt{8} \times$ “SGLI pixel size” (= 707 m), which indicates that a pixel at the center of this lake region usually consists of a signal purely from the lake surface (with no land component) (Oppenheimer 1993). Therefore, we can estimate the surface temperature of the lake water from SGLI pixel values taken from the lake center.

For the analysis of the lake surface temperature, we also used the radiative transfer equation-based method using the 10.8 μm band (e.g., Oppenheimer 1993) of the SGLI, instead of the split-window method, because we made the simultaneous comparison with the ground reference point (the temperature difference was tiny when we estimated the lake surface temperature on 21 June 2019 using these two methods; the radiative transfer equation-based method: 38.2 $^{\circ}\text{C}$, the split-window algorithm using the 10.8 and 12.0 μm bands: 38.0 $^{\circ}\text{C}$). The

time-series variation of the thermal anomaly was measured by selecting images without clouds over Ijen, and extracting the pixel with the highest value within a region of about 5 pixels \times 5 pixels around the location of the crater lake in each image. The pixel-integrated temperature of those pixels (T11Mx—indicating the actual temperature because the temperature distribution within the pixel is almost homogeneous) was used to identify thermal anomalies (Kaneko et al. 2018). As the surface temperature of the lake water might be affected by seasonal and diurnal variations of the surrounding environment, we measured the temperature of the neighboring inactive area at the same altitude as the Ijen crater lake (altitude of 2200 m, about 1.8 km north of Ijen) as the background temperature (T11Bk).

Results for 2019 Ijen activity

Figure 5c shows the SGLI image for 21 June. In the land area of the eastern end of Java Island seen here, the Ijen crater lake is found to be the hottest point. In the enlarged image of the summit area on the same day (Fig. 5d), we can recognize an area with temperatures higher than the surroundings, consisting of 4 to 5 pixels in the east–west and north–south directions, which almost matches the size of the lake. The temperature at the center of this thermal anomaly is the highest (corresponding to T11Mx), which is considered to indicate the surface temperature of the lake water.

Figure 5e shows the time-series variations of T11Mx and T11Bk. From January to April, T11Mx is around 18 $^{\circ}\text{C}$, slightly higher than the background; however, it rises from mid-May and reaches a maximum of 38 $^{\circ}\text{C}$ on 21 June. After that, T11Mx gradually decreases and remains almost constant from September to December. It does not return to the pre-May level but stays relatively higher, about 25 $^{\circ}\text{C}$. During the same period, T11Bk is almost constant. The Indonesia Centre for Volcanology and Geological Hazard Mitigation reported that the highest surface temperature of the lake water was 38 $^{\circ}\text{C}$ in June 2019 during the period between June 2019 and 14 January 2020 (CVGHM 2020). Their measurement matches our estimation using the SGLI. The lake temperature of Ijen is closely related to the magmatic or hydrothermal activities beneath the volcano, and it was observed in the range of 15–50 $^{\circ}\text{C}$ during 1991–2010 (Caudron et al. 2015). During active periods, the lake temperature often reaches 47–48 $^{\circ}\text{C}$ or higher (Caudron et al. 2015). During the 2019 activity, the lake water temperature increased to 38 $^{\circ}\text{C}$ at maximum, which was lower than the temperature observed during other active periods. This fact suggests that even if it was caused by underground magma or hydrothermal activity, the magnitude must have been small.

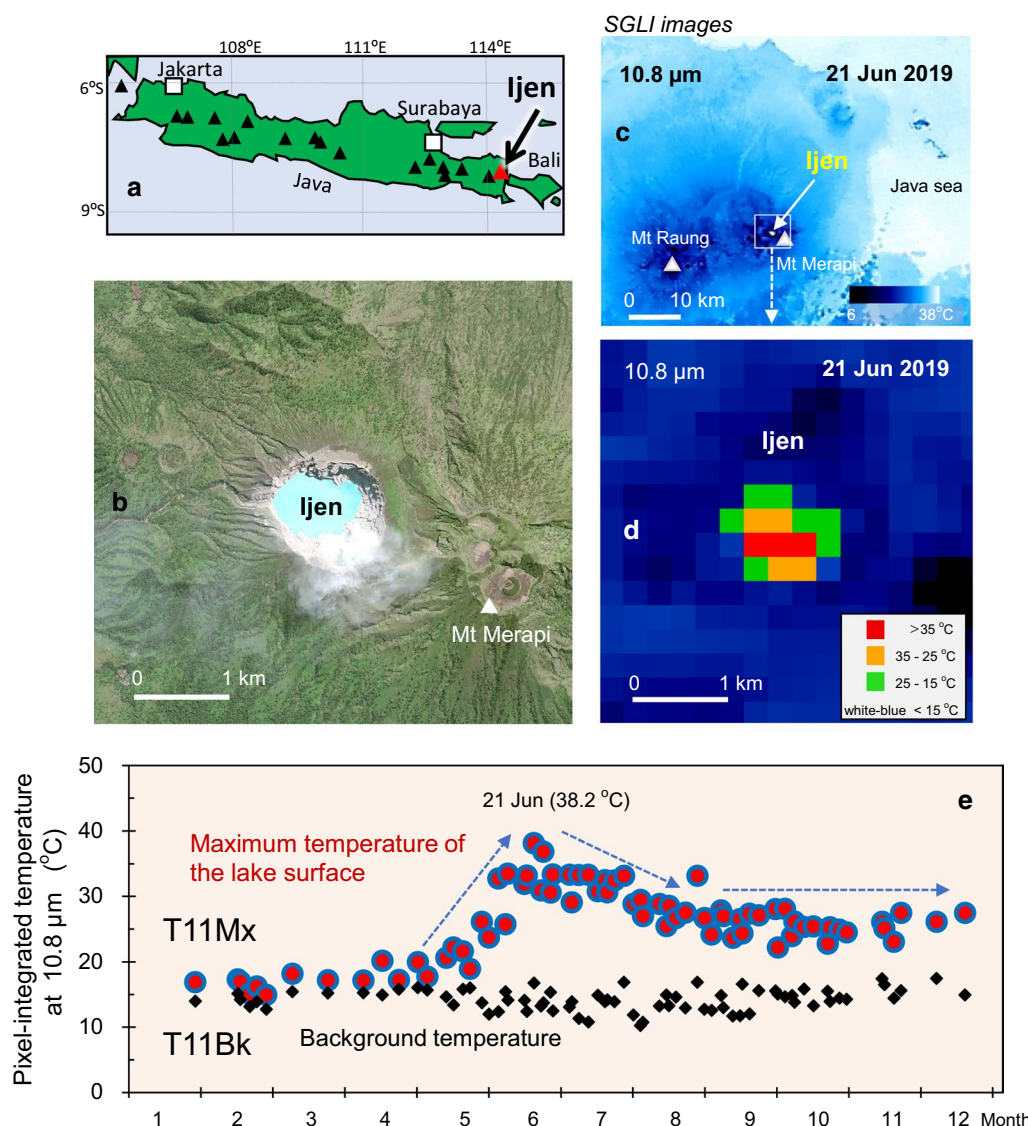


Fig. 5 **a** Location of Ijen. **b** Ijen and the surrounding areas (WorldView-2 image). **c** SGLI 10.8 μm image of 21 June 2019. The Ijen volcanic crater lake is found to be the hottest point in the image field. **d** Pixel-integrated temperature images of the SGLI 10.8 μm band in the vicinity of the Ijen volcanic crater lake on 21 June. **e** Time-series variations of thermal anomalies (T11Mx and T11Bk) detected by the 10.8 μm band of SGLI between January and December 2019

Discussion of 2019 Ijen activity

Based on the observations described above, if Ijen shifts to an active phase in the future, it is expected that the process can be monitored in detail by continuous observation of the surface temperature using the SGLI 10.8 μm band. Although the use of thermal infrared bands of high-resolution satellite images, such as those from the Landsat Thermal Infrared Sensor, is also possible, it may be difficult to detect the occurrence of a thermal anomaly that is systematic but low in level because the observation frequency is too low, every few weeks. Thanks to the

high-density observation, every 2–3 days, the SGLI can detect a slight difference even in low-level activity. Furthermore, in combination with the high real-time performance of the SGLI, it is possible to detect signs of volcanic activity in real time by measuring the surface temperature of the lake water, which is useful as information for disaster prevention. There are some other active volcanic crater lakes with a diameter of 700 m or more, such as Lake Nyos (Cameroon) or Crater Lake of Taar volcano (Philippines). We may use the SGLI 10.8 μm band to monitor them.

2019 Sakurajima activity—intermittent small-scale vulcanian eruptions

Outline of the 2019 Sakurajima activity and analytical points

Sakurajima is an active volcano with an altitude of 1117 m (Fig. 6a, b) located in the southern part of Kyushu, Japan, and it has had repeated medium- to large-scale eruptions every few hundred years, such as the Anei eruption (1779) and Taisho eruption (1914) (Kobayashi and Sasaki 2014). Activity consisting of small-scale vulcanian eruptions at Minamidake (Fig. 6c) has continued intermittently since 1955. At its peak, in 1985, 474 eruptions were recorded (Kobayashi and Sasaki 2014). The activity declined somewhat in 2016–2017, but it increased again slightly in 2018 (JMA 2019).

We analyzed the activity of Sakurajima from January to December 2019 using SGLI images, and examined whether it was possible to recognize the occurrence of small-scale vulcanian eruptions or an activity state that could cause vulcanian eruptions. The 1.63 μm and 10.8 μm bands of the SGLI were used for the analysis. In each image of Sakurajima, the pixels with the highest value out of the 61-pixel (latitude direction) by 41-pixel (longitudinal direction) area centering on the summit of Minamidake were extracted in both bands. The radiance value at 1.63 μm (R1.6Mx) and the pixel-integrated temperature at 10.8 μm (T11Mx) were used as indicators of a thermal anomaly.

Results for 2019 Sakurajima activity

Figure 6d, f shows the time-series variations of the thermal anomalies based on SGLI images. In the time-series variation of R1.6Mx, thermal anomalies are observed in January–May and September–December (Fig. 6d). The number of explosive eruptions reported by the Japan Meteorological Agency (JMA 2019) was high in January–July and September–December, and the amount of ashfall deposits was large in February–June and September–December (Fig. 6h, i) (JMA 2019). Their variations well match those of R1.6Mx. Conversely, T11Mx shows no thermal anomaly throughout the period (Fig. 6f). The 1.63 μm image from 15 November (Fig. 6e) clearly shows a thermal anomaly in the summit area. The 10.8 μm image (Fig. 6g) shows a slight thermal anomaly in the same location; the pixel-integrated temperature is at a background level, that is, the same as the surrounding sea surface. This fact indicates that the heat source is at a high temperature exceeding several hundred degrees Celsius but very small in size. At Sakurajima at this time, the radiance value in the 1.63 μm band is at most about $3 \times 10^6 \text{ W m}^{-2} \text{ sr}^{-1} \text{ m}^{-1}$ (Fig. 6d). If we assume that the temperature of the high-temperature heat source is 800 $^{\circ}\text{C}$, the size is estimated to be less than 0.1% ($\sim 63 \text{ m}^2$) of the SGLI pixel area (Fig. 1c). This estimate suggests

that this thermal anomaly may have been caused by the temporary exposure of a part of the magma head at the bottom of the craters (which may have also acted as a cap rock for a vulcanian eruption) (Fig. 6j).

Discussion of 2019 Sakurajima activity

Observations using the 1.63 μm band of the SGLI are considered to be useful for monitoring low-level activities caused by a small but high-temperature heat source. A vulcanian eruption is an explosive eruption that commonly occurs at volcanoes having highly viscous lava. In general, vulcanian eruptions are relatively small; however, they produce a vast number of projectiles and sometimes small pyroclastic flows. In such an eruption, people are at risk if they enter the areas near active craters (e.g., 1997 and 2000 Semeru). Constant real-time observation of such risky volcanoes using the 1.63 μm band of the SGLI to identify whether they have entered an active state that could cause vulcanian eruptions could contribute to reducing eruption casualties. For this purpose, the observation frequency must be higher than the current frequency of every 2–3 days.

Application to real-time monitoring—a powerful primary survey tool

We previously developed a real-time volcano observation system (called RealVOLC) using infrared images from satellites, such as the Advanced Very-High-Resolution Radiometer, MODIS, and Multifunctional Transport Satellites, and have been observing major active volcanoes in the Asia-Pacific region since 2001 (Kaneko et al., 2002b, 2010). In the late 2010s, new satellites, Himawari-8 and GCOM-C, were launched (JAXA, 2018a; JMA, 2017), and we have worked on developing a new system using data from these satellites. The new observation system will use SGLI images for real-time monitoring of the distribution of effused lava or pyroclastic materials, as well as the locations of eruption centers. In addition to the much higher resolution than MODIS (Fig. 1d, e) and other newer satellites, the SGLI has the advantage of high real-time performance, as well, which leads to high utility for disaster prevention.

Recently, we completed developing a prototype real-time monitoring system using SGLI as an extension of RealVOLC (<https://vrsserv.eri.u-tokyo.ac.jp/realvolc/>) and are performing trial operations. In this system, observation results are automatically uploaded to the Web site in real time (Fig. 7). In the Web-SGLI system, charts showing annual time-series variation of R1.6Mx and T11Mx as indicators of thermal anomalies (Kaneko et al., 2018) are shown alongside the latest images of the 1.63 μm and 10.8 μm bands. Presently, it takes approximately 13 h to display the analytical results on Web-SGLI

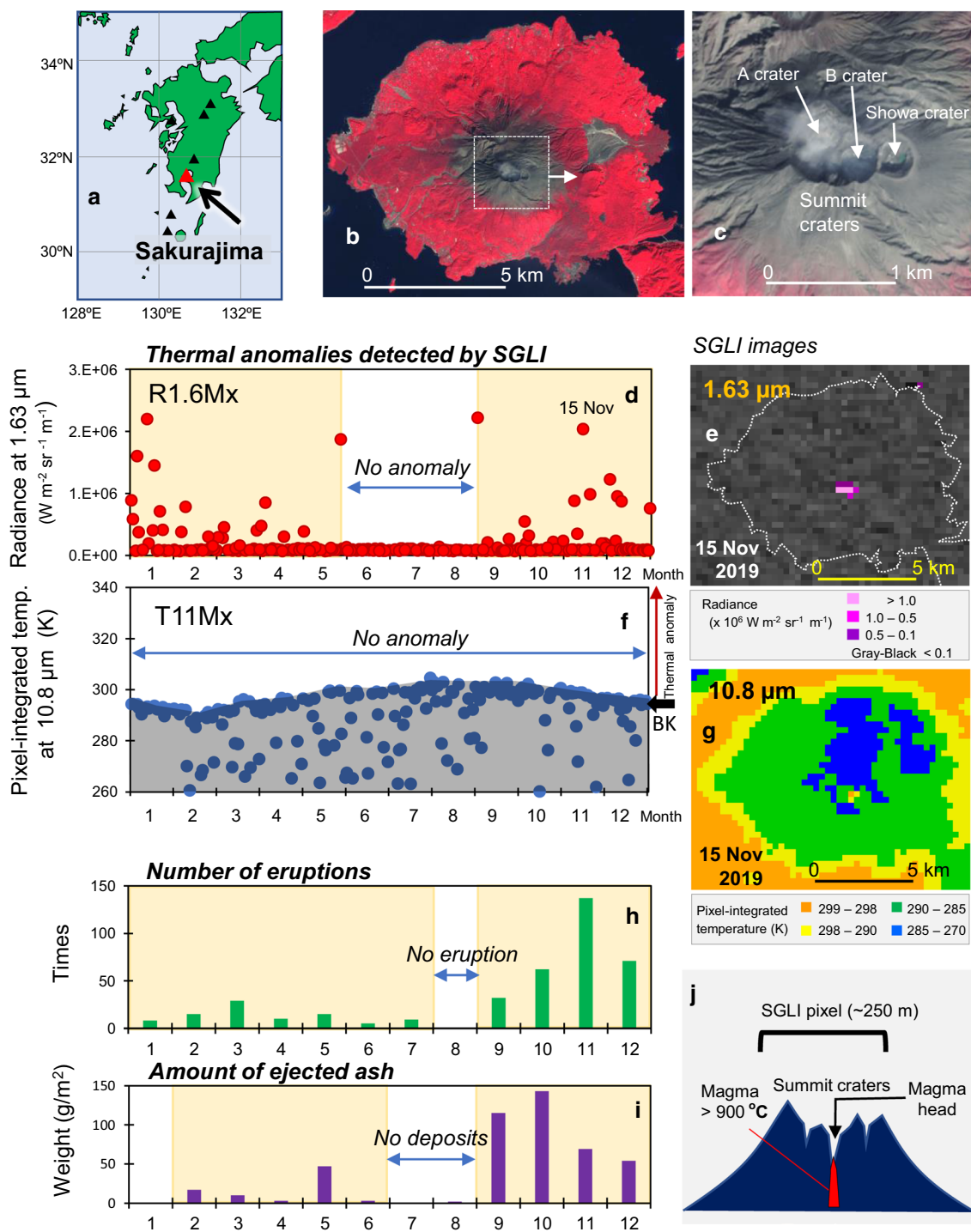


Fig. 6 **a** Location of Sakurajima volcano. **b** Topography of Sakurajima volcano (Sentinel-2 image). **c** Summit craters (Minamidake) of Sakurajima volcano (Sentinel-2 image). **d** Time-series variation of thermal anomaly (R1.6Mx) detected in the 1.63 μm band with the SGLI between January and December 2019. **e** SGLI 1.63 μm image of 15 November (radiance). **f** Time-series variation of thermal anomaly (T11Mx) detected in the 10.8 μm band with the SGLI between January and December 2019 (pixel-integrated temperature). **g** SGLI 10.8 μm image of 15 November. **h** The number of explosive eruptions reported by JMA (JMA, 2019). **i** Amount of ashfall deposits reported by JMA (JMA, 2019). **j** Possible model to explain the observation results obtained by the SGLI 1.63 and 10.8 μm images

after observation by the GCOM-C satellite (reducing this time is an objective of ongoing work). We plan to use this system for continuous monitoring of major active volcanoes in the Asia-Pacific region, to detect eruptions and analyze eruptive sequences in real time. For important eruptions, we will conduct detailed analyses by combining various satellite images and field observations as necessary (e.g., Kaneko et al. 2019a, b). The new real-time monitoring system using GCOM-C and Himawari-8 can be a powerful primary survey tool for eruptions. Using this system, we can perform a rapid and accurate analysis of eruptions, which is also useful for disaster prevention.

Conclusions and remarks

The analytical results of this study have demonstrated that GCOM-C SGLI images are significantly useful for observing various aspects of volcanic activity. The following points summarize the investigation results for the effective use and further potential for the 250 m resolution images from the SGLI to study eruptive activities.

1. Large-scale effusive activity: The scale of massive lava flows is much larger than the SGLI pixel size of

250 m. Thus, we can observe the distribution areas of a lava flow in detail with SGLI images in the 10.8 μm band. The method described here for creating a cumulative thermal anomaly map is useful for observing the enlargement process of lava flows.

2. The activity of lava dome growth and the generation of associated pyroclastic flows: We can effectively observe lava dome growth, and detect the generation of associated pyroclastic flows using SGLI images, due to the high observation frequency and reasonably high resolution of 250 m. The 1.63 μm band is suitable for observing the activity of a lava dome, while the 10.8 μm band is suitable for capturing the occurrence and the distribution of pyroclastic flows.

3. The activity of an active volcanic crater lake: We can observe the surface temperature of volcanic crater lakes having a diameter of 700 m or more with SGLI. The 10.8 μm band of SGLI is best for such measurement because it can detect a slight difference in the temperature variation due to the high-density observation. For these measurements, it is useful to measure the value of

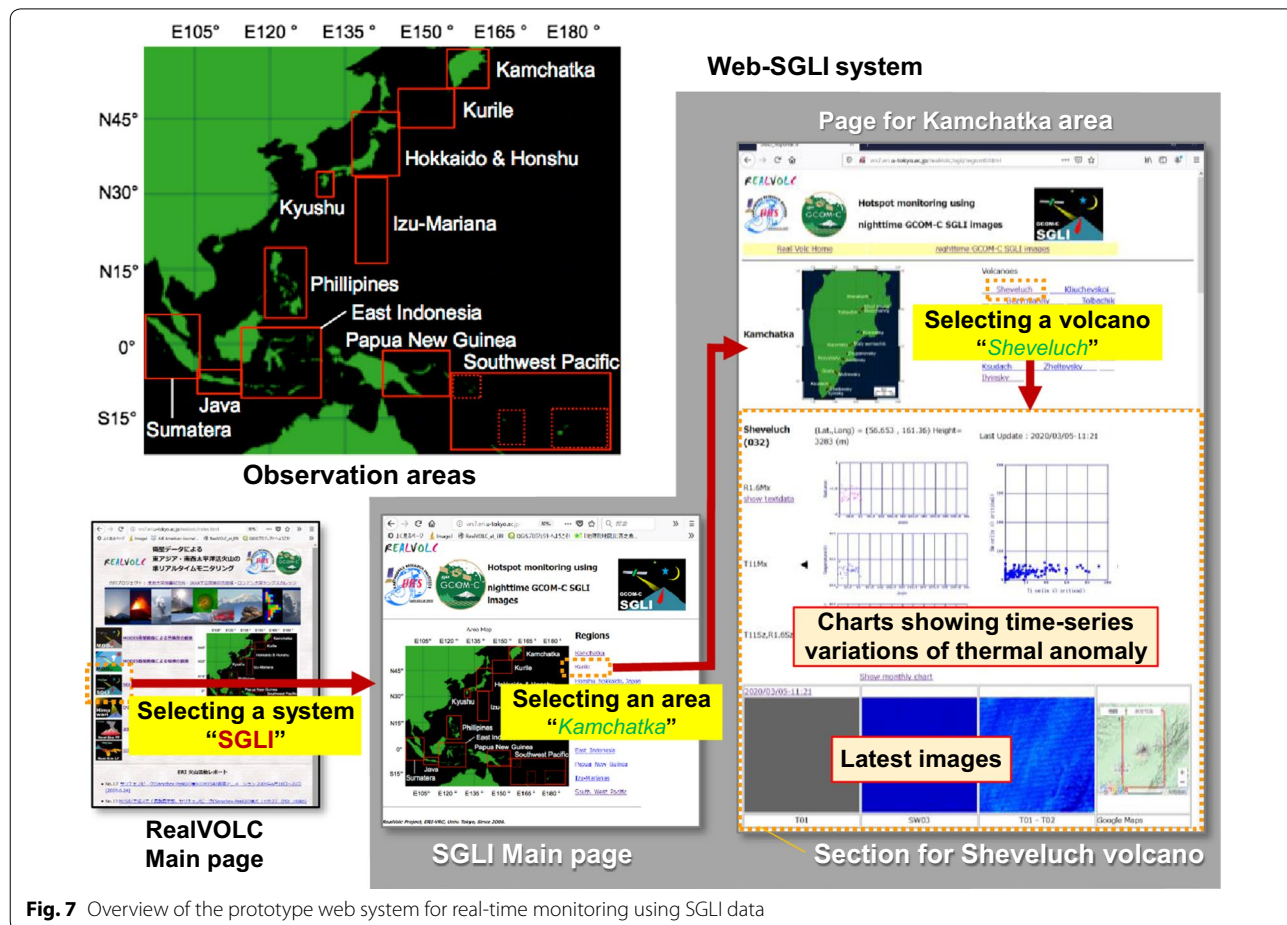


Fig. 7 Overview of the prototype web system for real-time monitoring using SGLI data

a neighboring inactive area at the same altitude and use it as a background.

4. Intermittent activities of small-scale vulcanian eruptions: The 1.63 μm band of SGLI is suitable for observing the intermittent activity of small-scale vulcanian eruptions. The 1.63 μm band is sensitive to a high-temperature heat source even if it is smaller than 0.1% of the pixel size of the SGLI. Thus, it can detect minimally exposed magma at the bottom of a vent, which is a potential cause of vulcanian eruptions. Using the 10.8 μm band concurrently, information on the properties of the heat source can be obtained.

5. By making it possible to view the observation results by SGLI in real time, it may be possible to reduce various types of eruption-related disasters. For this purpose, it is vital to develop and operate a real-time satellite observation system that includes SGLI data.

The SGLI does not have a mid-wavelength infrared band, such as 3.9 μm , with a resolution of 250 m; this band is frequently used for volcanic observations (e.g., Wright et al. 2004; Coppola et al. 2016). The lack of observations at this wavelength makes it difficult to detect small heat sources in the temperature range below a few hundred degrees Celsius (Fig. 1a, b). In the very early stages of an eruption, even if magma is not exposed in the crater, weak thermal anomalies may appear due to, for example, gas release, and mid-wavelength infrared signals are effective for detecting such thermal anomalies (Kaneko et al. 2018). In the next generation of GCOM-C, if the 2.21 μm band is improved to have 250 m resolution and a 3.9 μm band with 250 m resolution is added, these would be very powerful tools for detecting such phenomena. Because the SGLI is an optical sensor, it cannot make observations in cloudy conditions, which are very common in the Asia-Pacific region. Thus, it is vital to increase the frequency of observations. In the future, it is important to launch multiple GCOM-C satellites and establish a system that enables high-frequency observation by a satellite constellation.

Abbreviations

DN: Digital number; ERZ: East Rift Zone; GCOM-C: Global Change Observation Mission-Climate; IRS: Infrared scanning radiometer; JAXA: Japan Aerospace Exploration Agency; L2 LTOA: Level-2 top-of-atmosphere radiance; MODIS: Moderate Resolution Imaging Spectroradiometer; NN: Nearest neighbor; R1.6Mx: Spectral radiance of the pixel showing the maximum value in the heat source area in the 1.63 μm images; SGLI: Second-generation global imager; T11Bk: Pixel-integrated temperature of the pixel showing the background level in the 11 μm images; T11Mx: Pixel-integrated temperature of the pixel showing the maximum value in the heat source area in the 10.8 μm images; USGS: U.S. Geological Survey; VNR: Visible and near-infrared radiometer.

Acknowledgements

We thank the members of the GCOM-C Scientific team of JAXA, notably the late Y. Shimoda of Tokai University, M. Moriyama of Nagasaki University, K. Nasahara of Tsukuba University, M. Hori of Toyama University, and K. Tanaka of

JAXA for their encouragement and helpful suggestions. We also deeply appreciate R. Ohno for handling the SGLI data. Comments and suggestions from an anonymous reviewer and Y. Ogawa, editor-in-chief of EPS, of Tokyo Institute of Technology were hugely helpful for improving the manuscript.

Authors' contributions

Conceptualization, T.K.; methodology, A.Y.; software, K.T.; writing—original draft preparation, T.K.; writing—review and editing, T.K., S.N. and H.M.; supervision, T.F., Y.H., K.K. and H.M. All authors read and approved the final manuscript.

Funding

This work was supported by a Grant-in-Aid for Scientific Research from the Japan Society for the Promotion of Science, Kakenhi C (Grant No. 19K04011 to TK); second Research Announcement on the Earth Observations (PI No. ER2GCF111 to TK) from the Earth Observation Research Center of Japan Aerospace Exploration Agency; Earthquake and Volcano Hazards Observation and Research Program of the Ministry of Education, Culture, Sports, Science and Technology of Japan (No. ERL_07); and Cross-ministerial Strategic Innovation Promotion Program II – SIP II (Enhancement of Societal Resiliency against Natural Disasters). The Sentinel-2 images used here were provided by Sentinel Hub.

Availability of data and materials

The SGLI Level 1b images used in this study are available from the G-Portal website: <https://gportal.jaxa.jp/gpr/>.

Ethics approval and consent to participate

Not applicable.

Consent for publication

Not applicable.

Conflict of interest

The authors declare that they have no competing interests.

Author details

¹ Earthquake Research Institute, The University of Tokyo, 1-1-1 Yayoi, Bunkyo-ku, Tokyo 113-0032, Japan. ² Japan Fisheries Research and Education Agency, 2-12-4 Fukuura, Kanazawa, Yokohama, Kanagawa 236-8648, Japan. ³ The National Institute of Advanced Industrial Science and Technology (AIST), 1-1-1 Umezono, Tsukuba, Ibaraki 305-8560, Japan. ⁴ Mount Fuji Research Institute, 5597-1 Kenmarubi, Kamiyoshida, Fujiyoshida, Yamanashi 403-0005, Japan. ⁵ Center for Environmental Remote Sensing, Chiba University, 1-33 Yayoi-cho, Inage-ku, Chiba-shi, Chiba 263-8522, Japan. ⁶ Earth Observation Research Center (EORC), Japan Aerospace Exploration Agency (JAXA), 2-1-1 Sengen, Tsukuba, Ibaraki 305-8505, Japan.

Received: 5 May 2020 Accepted: 1 August 2020

Published online: 10 August 2020

References

- Belousov A, Belousova M, Voight B (1999) Multiple edifice failures, debris avalanches and associated eruptions in the Holocene history of Shiveluch volcano Kamchatka, Russia. *Bull Volcanol* 61:324–342. <https://doi.org/10.1007/s004450050300>
- Berk A, Bernstein LS, Robertson DC (1989) MODTRAN: a moderate resolution model for LOWTRAN 7, Tech Rep, GL-TR-89-0122, Geophys Lab, AFSC, Hanscom AFB, MA. <https://apps.dtic.mil/dtic/tr/fulltext/u2/a214337.pdf>. Accessed 1 May 2020
- Caudron C, Syahbana DK, Lecocq T, Van Hinsberg V, McCausland W, Triantafyllou A, Camelbeeck T, Bernard A (2015) Kawah Ijen volcanic activity: a review. *Bull Volcanol* 77:16. <https://doi.org/10.1007/s00445-014-0885-8>
- Coppola D, Laiolo M, Cigolini C, Delle Donne D, Ripepe M (2016) Enhanced volcanic hot-spot detection using MODIS IR data: results from the MIROVA system. In: Harris AJL, De Groeve T, Garel F, Carn SA (eds) *Detecting, modelling and responding to effusive eruptions*. *Geol Soc Lond Spec Publ* 426:181–205. <https://doi.org/10.1144/SP426.5>
- CVGHM (2020) Press release of Mt. Ijen volcanic activity, January 18, 2020. <https://vsi.esdm.go.id/index.php/gunungapi/aktivitas-gunung>

- [gapi/2858-press-release-aktivitas-vulkanik-g-ijen-18-januari-2020](#). (in Indonesian) Accessed 1 May 2020
- Edwards B, Belousov A, Belousova M, Volynets A, Melnikov D, Chirkov S, Senyukov S, Gordeev E, Muraviev Y, Izbekov P, Demianchuk Y (2013) Another "Great Tolbachik" Eruption? *Eos Trans Am Geophys Uni* 94:189–191. <https://doi.org/10.1002/2013EO210002>
- Feng K, Huang H, Wu Y (2020) Detecting pre-eruptive magmatic processes of the 2018 eruption at Kilauea, Hawaii volcano with ambient noise interferometry. *Earth Planets Space* 72(1):74. <https://doi.org/10.1186/s40623-020-01199-x>
- Harris AJL (2013) Thermal remote sensing of active volcanoes, a user's manual. Cambridge University Press, Cambridge
- Imaoka K, Kachi M, Fujii H, Murakami H, Hori M, Ono A, Igarashi T, Nakagawa K, Oki T, Honda Y, Shimoda H (2010) Global Change Observation Mission (GCOM) for monitoring carbon, water cycles, and climate change. *Proc IEEE* 98:717–734. <https://doi.org/10.1109/JPROC.2009.2036869>
- JAXA (2018a) GCOM-C "SHIKISAI" data users handbook, first edition. https://gportal.jaxa.jp/gpr/assets/mng_upload/GCOM-C/GCOM-C_SHIKISAI_Data_Users_Handbook_en.pdf. Accessed 1 May 2020
- JAXA (2018b) SGLI level 1 product format description, first edition. https://gportal.jaxa.jp/gpr/assets/mng_upload/GCOM-C/SGLI_Level1_Product_Format_Description_en.pdf. Accessed 1 May 2020
- JMA (2017) Himawari-8/9 Himawari standard data user's guide version 1.3. https://www.data.jma.go.jp/mscweb/en/himawari89/space_segment/hsd_sample/HSD_users_guide_en_v1.3.pdf. Accessed 17 May 2020
- JMA (2019) Volcanic activities of Sakurajima during 2019. https://www.data.jma.go.jp/svd/vois/data/tokyo/STOCK/monthly_v-act_doc/fukuo/ka/2019y/506_19y.pdf. (in Japanese) Accessed 1 May 2020
- Kaneko T, Maeno F, Yasuda A (2019) Observation of the eruption sequence and formation process of a temporary lava lake during the June–August 2015 Mt Raung eruption, Indonesia, using high-resolution and high-frequency satellite image datasets. *J Volcanol Geotherm Res* 377:17–329. <https://doi.org/10.1016/j.jvolgeores.2019.03.016>
- Kaneko T, Maeno F, Yasuda A, Takeo M, Takasaki K (2019) The 2017 Nishinoshima eruption: combined analysis using Himawari-8 and multiple high-resolution satellite images. *Earth Planets Space* 71(1):140. <https://doi.org/10.1186/s40623-019-1121-8>
- Kaneko T, Takasaki K, Maeno F, Wooster MJ, Yasuda A (2018) Himawari-8 infrared observations of the June–August 2015 Mt Raung eruption, Indonesia. *Earth Planets Space* 70(1):89. <https://doi.org/10.1186/s40623-018-0858-9>
- Kaneko T, Wooster MJ (1999) Landsat infrared analysis of fumarole activity at Unzen volcano: time-series comparison with gas and magma fluxes. *J Volcanol Geotherm Res* 89:57–64. [https://doi.org/10.1016/S0377-0273\(98\)00122-X](https://doi.org/10.1016/S0377-0273(98)00122-X)
- Kaneko T, Wooster MJ, Nakada S (2002) Exogenous and endogenous growth of the Unzen lava dome examined by satellite infrared image analysis. *J Volcanol Geotherm Res* 116:151–160. [https://doi.org/10.1016/S0377-0273\(02\)00216-0](https://doi.org/10.1016/S0377-0273(02)00216-0)
- Kaneko T, Yasuda A, Aoki Y, Kajiwara K, Kitagawa S (2010) Realtime monitoring of active volcanoes in East Asia using MODIS and MTSAT data and its advancement by GCOM-C1 SGLI, *International Archives of the Photogrammetry, Remote Sensing and Spatial Information Science XXXVIII(8)*: 209–212, Kyoto, Japan 2010. [http://www.tricu-tokai.ac.jp/ISPRScom8/TC8/TC8_CD/headline/PS-1\(WG%20VIII\)/W01P01_20100308200937.pdf](http://www.tricu-tokai.ac.jp/ISPRScom8/TC8/TC8_CD/headline/PS-1(WG%20VIII)/W01P01_20100308200937.pdf). Accessed 1 May 2020
- Kaneko T, Yasuda A, Ishimaru T, Takagi M, Wooster MJ, Kagiya T (2002) Satellite hot spot monitoring for Japanese volcanoes: a prototype AVHRR based system. *Advance Enviro Monit Model* 1:153–166
- Kobayashi T, Sasaki H (2014) Sakurajima Volcano. *J Geol Soc Japan* 120:63–78 (in Japanese)
- Krippner JB, Belousov AB, Belousova MG, Ramsey MS (2018) Parametric analysis of lava dome-collapse events and pyroclastic deposits at Shiveluch volcano Kamchatka, using visible and infrared satellite data. *J Volcanol Geotherm Res* 354:115–129. <https://doi.org/10.1016/j.jvolgeores.2018.01.027>
- Macdonald GA, Abbott AT, Peterson FL (1983) *Volcanoes in the Sea, the geology of Hawaii*, 2nd edn. University Hawaii Press, Honolulu
- Nakada S, Shimizu H, Ohta K (1999) Overview of 1990–1995 eruptions at Unzen Volcano. *J Volcanol Geotherm Res* 89:1–22. [https://doi.org/10.1016/S0377-0273\(98\)00118-8](https://doi.org/10.1016/S0377-0273(98)00118-8)
- Neal CA, Brantley SR, Antolik L, Babb JL, Burgess M, Calles K, Capps M, Chang JC, Conway S, Desmither L, Dotray P, Elias T, Fukunaga P, Fuke S, Johanson IA, Kamibayashi K, Kauahikaua J, Lee RL, Pekalib S, Miklius A, Million W, Moniz CJ, Nadeau PA, Okubo P, Parcheta C, Patrick MR, Shiro B, Swanson DA, Tollett W, Trusdell F, Younger EF, Zoeller MH, Montgomery-Brown EK, Anderson KR, Poland MP, Ball JL, Bard J, Coombs M, Dieterich HR, Kern C, Thelen WA, Cervelli PF, Orr T, Houghton BF, Gansecki C, Hazlett R, Lundgren P, Diefenbach AK, Lerner AH, Waite G, Kelly P, Clor L, Werner C, Mulliken K, Fisher G, Damby D (2019) The 2018 rift eruption and summit collapse of Kilauea Volcano. *Science* 363:367–374. <https://doi.org/10.1126/science.aav7046>
- Oppenheimer C (1993) Infrared surveillance of crater lakes using satellite data. *J Volcanol Geotherm Res* 55:117–128. [https://doi.org/10.1016/0377-0273\(93\)90093-7](https://doi.org/10.1016/0377-0273(93)90093-7)
- Oppenheimer C, Francis PW, Rothery DA, Carlton RWT, Glaze LS (1993) Infrared image analysis of volcanic thermal features: Láscar Volcano, Chile, 1984–1992. *J Geophys Res* 98:4269–4286. <https://doi.org/10.1029/92JB02134>
- Rothery DA, Francis PW, Wood CA (1988) Volcano monitoring using short wavelength infrared data from satellites. *J Geophys Res* 93:7993–8008. <https://doi.org/10.1029/JB093IB07p07993>
- Shevchenko AV, Dvigalo VN, Svirid IYu (2015) Airborne photogrammetry and geomorphological analysis of the 2001–2012 exogenous dome growth at Molodoy Shiveluch Volcano, Kamchatka. *J Volcanol Geotherm Res* 304:94–107. <https://doi.org/10.1016/j.jvolgeores.2015.08.013>
- Takada A, Yamamoto T, Ishizuka Y, Nakano S (2014) Geological map of Fuji Volcano, Second edition (ver.1). GSJ Open-F Rep 592, Geological Survey of Japan, AIST (in Japanese with English Abstract)
- Tanaka K, Okamura T, Amano T, Hiramatsu M, Shiratama K (2010) Operation concept of the second-generation global imager (SGLI), Proc SPIE 7862, earth observing missions and sensors: development, implementation, and characterization, 786209, Incheon, South Korea, 4 Nov 2010. 10.1117/12.869398.
- Tanaka K, Okamura Y, Mokuno M, Amano T, Yoshida J (2018) First year on-orbit calibration activities of SGLI on GCOM-C satellite, Proc SPIE 10781, Earth observing missions and sensors: development, implementation, and characterization V, 107810Q, Honolulu, Hawaii, 23 Oct 2018. 10.1117/12.2324703.
- Tanaka K, Okamura Y, Amano T, Hosokawa T, Uchikata T (2014) The development status of Second Generation Global Imager (SGLI), Infrared Scanning Radiometer (SGLI-IRS), Proc SPIE 9264, Earth observing missions and sensors: development, implementation, and characterization III, 92640G, Beijing, China, 19 Nov 2014. 10.1117/12.2073597.
- USGS (2018) Kilauea, Maps. https://volcanoes.usgs.gov/volcanoes/kilauea/multimedia_maps.html. Accessed 1 May 2020
- Walter LS, Salisbury JW (1989) Spectral characterization of igneous rocks in the 8- to 12- μ m region. *J Geophys Res* 94:9203–9213. <https://doi.org/10.1029/JB094iB07p09203>
- Wooster MJ, Kaneko T (1998) Satellite thermal analysis of lava dome effusion rate at Unzen Volcano, Japan. *J Geophys Res* 130:20935–20947. <https://doi.org/10.1029/97JB03392>
- Wooster MJ, Rothery DA (1997) Thermal monitoring of Láscar volcano, Chile, using infrared data from the along-track scanning radiometer: a 1992–1995 time series. *Bull Volcanol* 58:566–579. <https://doi.org/10.1007/s004450050163>
- Wright R, Flynn L, Garbeil H, Harris AJL, Pilger E (2004) MODVOLC: near-real-time thermal monitoring of global volcanism. *J Volcanol Geotherm Res* 135:29–49. <https://doi.org/10.1016/j.jvolgeores.2003.12.008>
- Wright HMN, Bernard B, Ramon P, Guevara A, Hidalgo S, Pacheco DA, Narváez D, Vásquez F (2015) Preliminary results on the 2015 eruption of Wolf Volcano, Isabela Island, Galápagos: chronology, dispersion of the volcanic products, and insight into the eruptive dynamics. Abstract V31B-3022, 2015 fall meeting, AGU, San Francisco, 14–18 Dec. <https://ui.adsabs.harvard.edu/abs/2015AGUFM.V31B3022W/abstract>. Accessed 1 May 2020.

Publisher's Note

Springer Nature remains neutral with regard to jurisdictional claims in published maps and institutional affiliations.